3D Image Reconstruction of a Fossil Using Neutron Tomography

A Major Qualifying Project (MQP) Report
Submitted to the Faculty of
WORCESTER POLYTECHNIC INSTITUTE
in partial fulfillment of the requirements
for the Degree of Bachelor of Science in

Physics
and Mathematical Sciences,

By:

Augustine Benjamin
Scarlett Clarke

Project Advisors:

Dr. Vadim V. Yakovlev
Dr. David C. Medich

Sponsored By:

Paul Scherrer Insitute

Date: January 25th, 2024

Abstract

Non-Destructive Testing (NDT) is an interdisciplinary field encompassing various inspection techniques and principles not compromising the structural integrity of the tested objects. NDT is commonly used in medicine, mechanical engineering, materials science, and numerous applications. Neutron imaging is a very efficient tool of NDT: contrary to X-rays, neutrons, when passing through the sample, are attenuated in accordance with the sample's composition or geometrical form and produce contrasts made by light materials (e.g., hydrogen, carbon, lithium). This characteristic gives neutron imaging a particular advantage when it comes to 3D visualizations. Neutron computed tomography (NCT) found its use in visualizing the inner structure of industrial, biological, geological, engineering, and other samples of interest.

In this project, a unique small fossil appearing as the vertebral column of an unknown pre-historic animal embedded in sandstone was investigated with the use of NCT. The fossil was found in the Morrison formation in Wyoming by the expedition of the Swiss Aathal Dinosaur Museum. The work in 3D image reconstruction was performed at the Swiss spallation source SINQ of the Paul Scherrer Institute (PSI) (Villigen, Switzerland). The fossils was exposed to a neutron beam, and the contrasts thus obtained were post-processed with the use of mathematical methods assuming the exponential law of radiation attenuation (the Beer–Lambert law) and using the Radon transform of the distribution of the linear neutron attenuation. Implementations of these methods in the three pieces of software, ImageJ, MuhRec, and Avizo, were used for visualization of the fossil.

A high-resolution 3D image of the sandstone block with the embedded vertebral column of the unknown animal was successfully obtained. The image seems to be showing all parts of bones and ribs hidden inside the sandstone block. However, the initial analysis was inconclusive as it was not possible to identify, based on the visible set of bones, the animal behind this fossil. The image, along with the materials documenting the full process of visualization, was passed to the Aathal Dinosaur Museum for more detailed investigation with the help of external paleontologist with relevant expertise.

The project was done in the WPI Switzerland Project Center in Zurich.

Acknowledgements

We would like to thank those who gave us the opportunity to participate in this project, and with whose guidance we have added to it:

- Professor Vadim Yakovlev for involving us in the project in the first place, and helped us to refine and polish this report from beginning to end.

- Professor David Medich for his support in our preparation for the project, and for his guidance during the project and writing this report.

- Dr. Pavel Trtik for his day-to-day support in learning the operation of NEUTRA, helping us with his expertise in tomography and imaging, and our guide for learning how to live and get around in Switzerland.

- Dr. Hans-Jakob Siber, Dr. Yolanda Schicker-Siber and Nils Knötschke of The Aathal Dinosaur Museum, for the preparation of the fossil, their expertise on the fossils on which we worked and for use of the fossil itself.

- Dr. Robert Zboray of EMPA for allowing us to make use of and his assistance with the X-ray imaging facilities there.

- Professor Nancy Burnham and the WPI Switzerland Project Center in Zurich for securing us housing and services while we did our project abroad.

Contents

List of Figures

1 Introduction

In summer 2022, during their expedition to the sandstone Morrison formation in south-central Wyoming, the Aathal Dinosaur Museum (in Aathal Valley, canton of Zurich, Switzerland) found a small piece of fossil delicately embedded in a piece of sandstone, seen in Figure 1. Only the vertebral column is visible on its surface, and it is unknown what creature is embedded in it. One possible hypothesis is that the fossil is a snake. If it is, this would be the oldest fossil of a snake currently known [Caldwell et al., 2015], making it incredibly precious. One other possibility is that the fossil is of a Sphenodontian reptile, a family with few un-fragmented fossils and only one living member, the New Zealand Tuatara [Siber, 2023]. Identifying the creature requires seeing the full shape of the fossil inside the sandstone matrix. Typically this is achieved by preparing the fossil using various mechanical and chemical techniques [Bevitt, 2018], but these interventions were inappropriate for this sample.

Chemical preparations involve acetic acid, and can damage the surface of the preserved bone. Mechanical preparation techniques use small hand tools, air engravers, and rotary tools which risk breaking or cutting away small bone pieces entirely [De Beer, 2017]. Replacement fossils are not obtainable. For any given time period, only the fossils that are currently in the earth are obtainable, and each is a unique portion of the prehistoric record. This fossil in particular is too thin and set too deeply in the surrounding sandstone to avoid these risks completely, and it is unusually large and complete, which makes it imperative to keep as much of the bone as possible. However, with the aid of an appropriate non-destructive visualization technique, identification may

Figure 1: Four samples of the Aathal Dinosaur Museum's fossil.

be possible, and with a 3D model of the bones' position within the sandstone, it would be easier to mechanically prepare the sample while avoiding damaging the bone, enabling a more certain identification and a better appreciated fossil.

As non-destructive testing (NDT) is apparently mandatory for being able to image the fossil without damaging it in exactly the way that the Aathal Dinosaur Museum wished to avoid, Neutron Computed Tomography (NCT) [PSI, 2023], [Schillinger et al., 2000], [Bilheux et al., 2015] appears to be a particularly attractive technique here. The basic principle of NCT is similar to that of X-ray radiography, but neutrons interact with the atoms' nuclei rather than with their electrons. A beam of neutrons passes through the sample and is attenuated in accordance with the sample's composition or its geometrical form. Also, contrary to X-rays, neutrons are attenuated by some light materials (such as hydrogen, carbon, and lithium). These characteristics give NCT, the combination of neutron imaging with suitable mathematical and computational tools for image processing and reconstruction, a big advantage for 3D visualizations of the considered set of fragile bones hidden within the sandstone matrix.

This report presents the output of the project in 3D image reconstruction of the Aathal
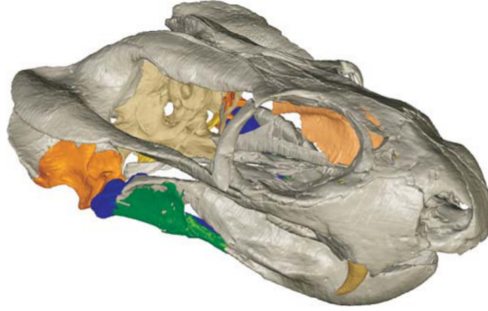
Figure 2: 3D model of a Pristerodon mackayi skull [Laaß, 2015b].

Dinosaur Museum's fossil with the use of NCT. The imaging was performed at the Swiss spallation source SINQ of the Paul Scherrer Institute (PSI) (Villigen, canton of Aargau, Switzerland). The sample was imaged in the PSI's NEUTRA beamline, and the image was post-processed with the use of ImageJ, MuhRec, and Avizo, three pieces of software used at PSI to generate visuals from contrasts obtained with the neutron beam. Mathematical methods involved in the image reconstruction are based on the exponential law of radiation attenuation (the Beer–Lambert law) and the Radon transform of the unknown distribution of the linear neutron attenuation. For better understanding of the output of neutron imaging, the sample also underwent X-ray scanning, which was performed at The Swiss Federal Laboratories for Materials Science and Technology (EMPA) (Dübendorf, canton of Zurich, Switzerland).

After corresponding tomographic reconstruction, segmentation, and visualization of the neutron-generated contrasts, a holographic 3D view of the sandstone block with the embedded vertebral column of the unknown animal was successfully obtained. The image is characterized by high resolution and seems to be showing all parts of bones and ribs hidden within the sandstone block. However, the picture appears to be inconclusive: it is difficult to immediately identify, based on the visible set of bones, the animal behind this fossil. The image was therefore passed to the Aathal Dinosaur Museum for their more detailed investigation to be held with the help of external paleontologists with relevant expertise.

1.1 Previous Studies

Other usages of neutron tomography in paleontology and other cultural heritage research projects have focused on objects whose composition make them a poor choice for X-ray analysis. Usually, this involves a hollow object made of ceramic or metal, or object–typically a fossil–embedded inside of a material that contains a large number of heavy atoms.

Previous researchers have used NCT to look at pre-prepared items in the past. Laaß [Laaß, 2015b] used NCT to look at the inside of a Pristerodon mackayi's skull cavity as seen in Figure 2. Using features from both the inside and outside of the skull enables more precise identification, and these features are also an additional way to track the cranial evolution. Grellet-Tinner [Grellet-Tinner et al., 2011] used the same technique on the first complete Titanosaur embryo fossilized along with its egg. It is neutron tomography that uncovered the presence of the Titanosaur embryo, and then enabled them to learn more about Titanosaur distribution patterns.

Paleontologists frequently have to deal with fossils embedded in chalk rock or "red" soil beds, so-called due to the high iron content coloring it. Neutron imaging is indifferent to these materials, instead contrasting the hydrogenous material of the fossil with its surroundings. Archaeologists and historians who have to deal with hollow ceramic and metal objects can use neutron imaging to scan the inside for organic/hydrogenated material, safely examining them without breaking them. This makes an additional argument in favor of neutron imaging as a preferable alternative to X-ray imaging in these circumstances [Schillinger et al., 2018].

Similarly to Laaß [Laaß, 2015b], Pugliesi [Pugliesi et al., 2019] used neutron tomography to gain a better view of the bones inside of a previously identified fish fossil. One may expect that the once-organic composition of the concretion would make the contrast between it and the fossil very poor, but they were still able to get a very distinct contrast for their sample, as seen in Figure 3.

A few papers have compared X-ray and neutron tomography head-to-head to find the pros and cons of both. [Karch et al., 2017] uses both technologies to perform computed tomography scans of a pair of fossils: a lignified, partly limonitized fossil ovuliferous cone of Fricia nobilis preserved in solid block of sandy marlstone and a silicified cone-like Dammarites albens stem.
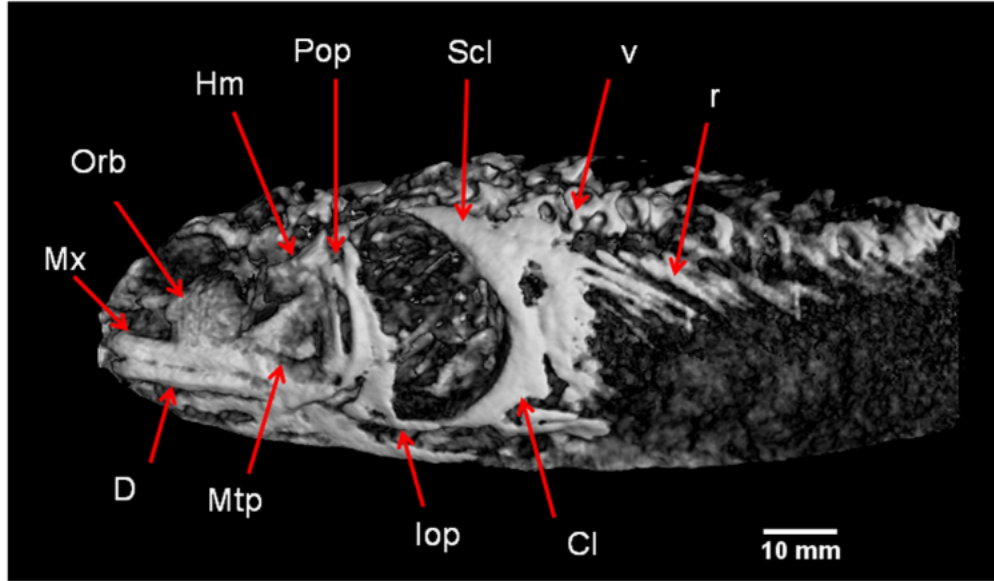
Figure 3: Neutron tomography slice of Notelops brama [Pugliesi et al., 2019].

They found that neutron imaging was able to reveal the surface structure of the Dammarites albens stem, distinguishing it from the surrounding sediment, as opposed to just showing the harder seeds embedded inside of the stem. They found that other features were much the same between X-ray and neutron techniques. [Laaß, 2015b] also has done a similar experiment on the fossils of non-mammalian synapsids [Laaß et al., 2017]. Synapsid fossils provide some illumination on early mammalian evolution. However, distinguishing them relies on distinguishing the shapes of their skeletons, and frequently only the outsides of these skeletons, as the insides are frequently filled in and inaccessible. Computed tomography can be used to image the hollows inside of the bones, and any structures of bone not easily visible from the outside of the fossil. This opens up many options in distinguishing and identifying synapsid fossils, and consequently in research on early mammalian evolution.

As evidenced from the short review above, the choice of NCT for NDT of the Aathal Dinosaur Museum's delicate fossil in a sandstone block was well motivated and natural. The neutron beamlines at PSI (one of them, NEUTRA, is shown in Figure 4) are known for successful projects in neutron tomography of diverse objects including artefacts related to cultural heritage and paleontological objects [Laaß, 2015a]. Neutron contrasts collected at the PSI beamlines can be conveniently post-processed with the use of advanced computational tools and converted to 3D
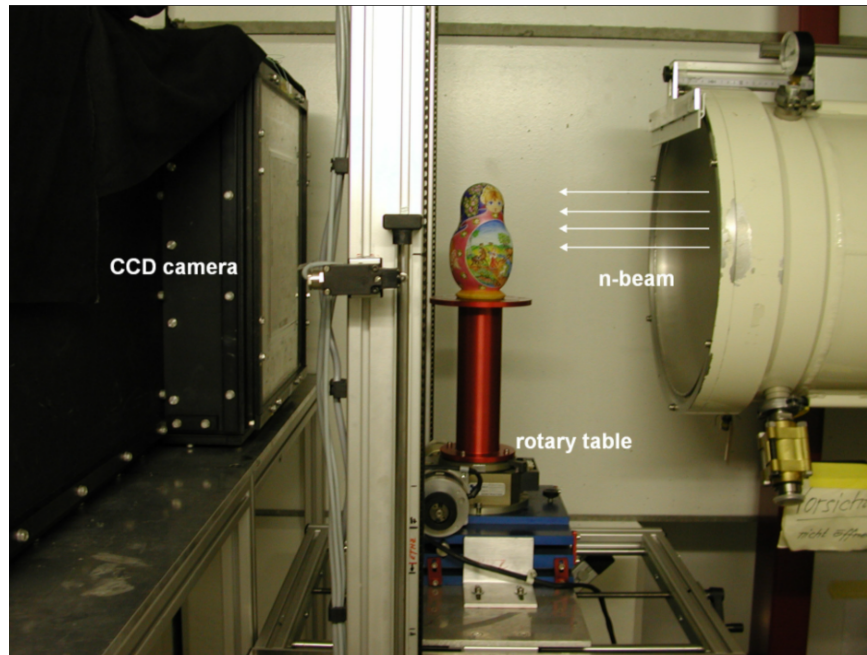
Figure 4: Experimental setup for neutron tomography at NEUTRA (Photo credit at [PSI, 2023].)

holographic images which were expected to help identify the animal behind the fossil hidden within the sandstone block in question.

1.2 Project Objectives

The goals of this project are therefore as follows:

1. Form projections of samples A-D using the neutron beamline NEUTRA

2. Construct a 3D image of the inside of the fossil from these 2D projections, using advanced techniques for image reconstruction in neutron tomography available at PSI.

3. Successfully distinguish (or segment) the bone from the surrounding material in the reconstructions.

4. Make a 3D model clearly displaying the bone inside each sample for use in identification.

2 Background

2.1 Tomography

In brief, tomography is the process of taking many images/projections through a subject as it rotates about an axis and reconstructing 3D image data from these projections, as is shown in Figure 5. To do this, the radial projection data is stored in a sinogram for each horizontal slice of the sample. The sinogram is a brightness map for a given y value, the brightness along the x axis is taken and mapped onto the new x axis of the sinogram. This is repeated for each θ step, and the corresponding images are used to reconstruct the slices.

Filtered Back projection is used to reconstruct each slice and obtain a 3D reconstruction. The brightness plot for a given θ on the sinogram is projected onto a dark image. This brightness data is then smeared across the blank image at an angle given by θ. An example of this process done with the same data, but differing quantities of θ steps is shown in Figure 6. The resulting image is then filtered and the smearing is repeated for the next θ step [Treimer, 2009].

2.2 Mathematical Foundations of Tomography

The geometric setup for the beam is shown in Figure 5 with the z coordinate being in the direction of the neutron's travel. The sample rotates some angle θ in the beam. A 2D projection image of the sample is taken at each angle. The final intensity of the beam after taking some path through the sample and striking some portion of the viewport is given by Beer's law, shown in Equation

7

Projection for a given θ
Brightness given by (θ,x,y)
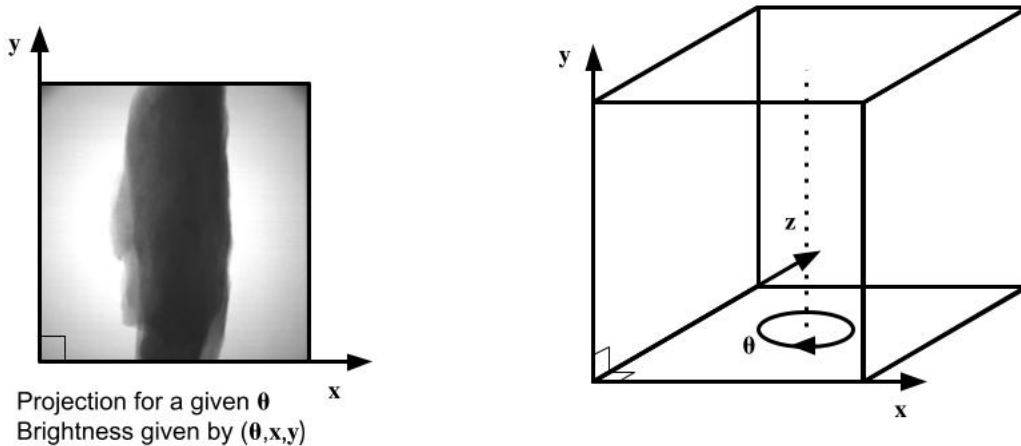
Figure 5: Coordinate axes used on the NEUTRA beamline.

(1), as a function of the path the beam has taken through the sample, with I as the final intensity, I_0 as the initial intensity of the beam along some path, and μ as a scalar field representing the attenuation coefficient of the material relative to the radiation in the beam:

$$I = I_0 \exp\left(-i \int \mu(x, y, z)dz\right) \tag{1}$$

Beer's law can be used to make an equation that associates a path through the sample with a real value:

$$\frac{I}{I_0} = \exp\left(-\int \mu(x, y, z)\,\mathrm{d}z\right)$$

$$\ln\left(\frac{I}{I_0}\right) = \int \mu(x, y, z)\,\mathrm{d}z$$

This is an example of a Radon Transform, which has a few mathematical properties that are useful for extracting the original attenuation coefficient μ from the tomography projections. The following section will cover this application.

Figure 6: A depiction of back-filter processing at 1, 2, 4, and 1000 projections [Treimer, 2009].

2.2.1 The Radon Transform

Since the beam is well-collimated, each path cutting through the sample is a line parallel to the z-axis, which will be parameterize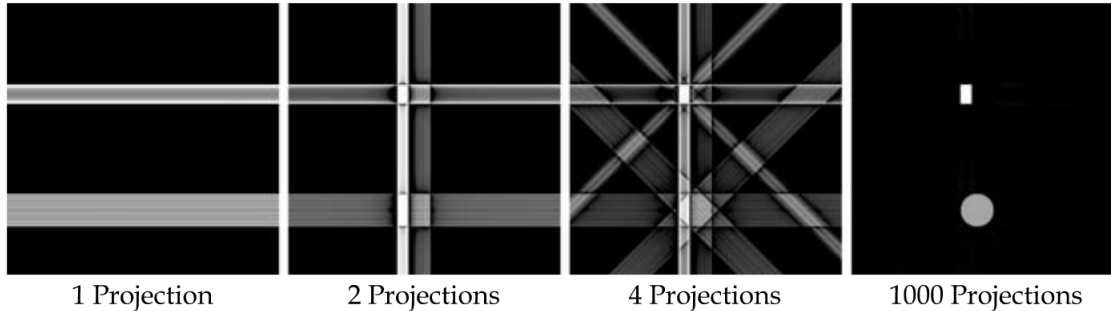d in z. Consider each plane cutting through the sample perpendicular to the axis of rotation. Each line in this plane that cuts through the sample is, at some angle, associated with a point on the projection for that angle.

The Radon Transform takes a function, and associates a scalar value to every line through its domain. In this case the domain of the function is $\mathbb{R}^2$, and the paths can be parameterized through it with two coordinates t and θ. This refers to the line perpendicular to the vector $(t\cos\theta, t\sin\theta)$ passing through that point.

With this parameterization in hand, the Radon Transform is the mathematical representation of the physical process of Tomography. Tomography works by taking images radially around an object. Images are taken by transmitting a particle, in this case a neutron, as the neutrons pass through the material. Some are absorbed or scattered away. The probability of a neutron passing through a cross-section of the material is dependent on the material. In a composite, a summation is done along the neutron's path to find the total probability of a neutron transmitting. With a well-collimated beam, the neutrons will pass through the sample in straight, parallel lines. This process is repeated radially on different angles around the sample.

It is used to represent the output data of a tomographic projection. The Radon Transform is $\mathcal{R} : \mathbb{R} \times [0, \pi) \mapsto \mathbb{R}$ (The general Radon transform is complex, but in this case the value is an intensity of radiation, which can only be real-valued.) In other words, the Radon Transform of a function takes that function, and assigns to each line lying in the function's domain a value equal

9

to the integral of the function over that line. It is given by the equation:

$$\mathcal{R}f(t,\theta) = \int_{L_{t,\theta}} f(\vec{x})\,\mathrm{d}S(\vec{x}) = \iint f(\vec{x})\delta(\langle\vec{x},\vec{\eta}_\theta\rangle - t)\,\mathrm{d}\vec{x} \tag{2}$$

where $\vec{\eta}_\theta = (\cos\theta, \sin\theta)$ and $L_{t,\theta} = \{\vec{x} : \langle\vec{x},\vec{\eta}_\theta\rangle = t\}$. For some chosen θ, an orientation of the sample, it is said $\mathcal{R}f(t,\theta) = \mathcal{P}_\theta(t)$ is the projection. This is identical to the tomography projection. In order to reconstruct from $\mathcal{P}_\theta(t)$ into the original input, it is necessary to complete an Inverse Radon Transform, in order to go from $\mathcal{P}_\theta(t)$ to the original function $\mu(x,y,z)$.

2.2.2 Projection Slice Theorem

To show that this is possible, and how to go about doing it, it is necessary to use the Projection Slice Theorem, also called the Fourier Slice Theorem. This theorem states that $\forall\theta \in [0,\pi)$:

$$\int \mathcal{R}f(t,\theta)e^{-i\omega t}\,\mathrm{d}t = \hat{f}(\omega\cos\theta, \omega\sin\theta) \tag{3}$$

In simple terms this states that "measuring the Radon transform is equivalent to acquiring the Fourier transform of f along radial lines" [Candes, 2021]. An illustrative proof is given below:

$$\int \mathcal{R}f(t,\theta)e^{-i\omega t}\,\mathrm{d}t = \int \iint f(\vec{x})\delta(\langle\vec{x},\vec{\eta}_\theta\rangle - t)e^{-i\omega t}\,\mathrm{d}\vec{x}\,\mathrm{d}t = \iint f(\vec{x})e^{-i\omega\langle\vec{x},\vec{\eta}_\theta\rangle}\,\mathrm{d}\vec{x} = \hat{f}(\omega,\vec{\eta}_\theta)$$

2.2.3 Inverse Radon Transform

Since there is no clean method to invert the Radon Transform, the first attempt is to try averaging $\mathcal{R}(t,\theta)$ on all lines containing $\vec{x}$ to find $f(\vec{x})$. It is noted that $\vec{x} \in L_{t,\theta}$ if and only if $t = \langle\vec{x},\vec{\eta}_\theta\rangle$. This method is called Back Projection [Candes, 2021], representing it by the equation:

$$\tilde{f}(\vec{x}) = \frac{1}{\pi}\int_0^\pi \mathcal{R}f(\langle\vec{x},\vec{\eta}_\theta\rangle,\theta)\,\mathrm{d}\theta \tag{4}$$

where $\mathcal{P}_\theta(t) = \mathcal{R}f(t,\theta)$. The issue with the resulting data is that it gives a blurry or imprecise reproduction of the original data. The data can be sharpened with the Projection Slice Theorem.

The Projection Slice Theorem states that a transform along radial lines is equivalent to what has been done with the line integrals, which means the two can be substituted. This process is also used in Back Projection.

2.2.4 Convolution Theorem

The Convolution Theorem states that taking the convolution of two functions and then taking the transform of the result is equivalent to taking the Fourier transform of each function and taking the product, as shown below. Given functions $G(s) = \mathcal{FT}[g(s)]$ and $H(s) = \mathcal{FT}[h(s)]$,

$$G(s)\dot{H}(s) = \mathcal{FT}[g(s) * h(s)] \tag{5}$$

where $*$ denotes a convolution. Since, for the Filtered Back Projection, a Fourier transform of the product of two functions is taken, this theorem can be used and a convolution taken instead, removing that Fourier transform and simplifying the process computationally.

2.2.5 Filtered Back Projection

The Filtered Back Projection equation is

$$f(x) = \frac{1}{2\pi} \int_0^\pi (\mathcal{R}f(t,\theta) * h\langle \vec{x}, \vec{\eta}_\theta \rangle \, \mathrm{d}\theta \tag{6}$$

where $*$ denotes a convolution over the kernel h. As seen below, a function $h(t)$ is required such that $FT^{-1}[\|r\|] = h(t)$. There is in fact no particular function satisfying this relation, but since there is non-continuous data, with values at only certain points, it is sufficient to find functions that are "close enough" at these points.

$$f(\vec{x}) = FT[\hat{f}(\vec{x})] = \frac{1}{(2\pi)^2} \int \int \hat{f}(\vec{\omega}) e^{i\langle \vec{\omega}, \vec{x} \rangle} \, \mathrm{d}\vec{\omega}$$

$$= \frac{1}{(2\pi)^2} \int_0^{2\pi} \int_0^\infty \hat{f}(r\vec{\eta}_\theta) e^{ir\langle \vec{\eta}_\theta, \vec{x} \rangle} r \, \mathrm{d}r \, \mathrm{d}\theta$$

$$= \frac{1}{(2\pi)^2} \int_0^\pi \int_0^\infty \hat{f}(r\vec{\eta}_\theta)e^{ir\langle\vec{\eta}_\theta,\vec{x}\rangle}r\,\mathrm{d}r\,\mathrm{d}\theta + \frac{1}{(2\pi)^2}\int_\pi^{2\pi}\int_0^\infty \hat{f}(r\vec{\eta}_\theta)e^{i\langle\vec{\eta}_\theta,\vec{x}\rangle}r\,\mathrm{d}r\,\mathrm{d}\theta$$

The second integral term can be represented in a more convenient form after a pair of u-substitution, here done as $\rho = -r$ and $\theta = \phi - \pi$:

$$\int_0^\pi \int_0^\infty \hat{f}(\rho\vec{\eta}_\phi)e^{i\rho\langle\vec{\eta}_\phi,\vec{x}\rangle}\rho\,\mathrm{d}\rho\,\mathrm{d}\phi = \int_\pi^{2\pi}\int_0^{-\infty}\hat{f}(-r\vec{\eta}_\phi)e^{-ir\langle\vec{\eta}_\phi,\vec{x}\rangle}(-r)\,\mathrm{d}(-r)\,\mathrm{d}\phi$$

$$= \int_\pi^{2\pi}\int_{-\infty}^0 \hat{f}(r\vec{\eta}_{\phi-\pi})e^{ir\langle\vec{\eta}_{\phi-\pi},\vec{x}\rangle}(-r)\,\mathrm{d}r\,\mathrm{d}\phi$$

$$= \int_0^\pi \int_{-\infty}^0 \hat{f}(r\vec{\eta}_\theta)e^{ir\langle\vec{\eta}_\theta,\vec{x}\rangle}(-r)\,\mathrm{d}r\,\mathrm{d}\theta$$

Thus the two integrals are combined as follows:

$$f(\vec{x}) = \frac{1}{(2\pi)^2}\int_0^\pi \int_0^\infty \hat{f}(r\vec{\eta}_\theta)e^{ir\langle\vec{\eta}_\theta,\vec{x}\rangle}r\,\mathrm{d}r\,\mathrm{d}\theta + \frac{1}{(2\pi)^2}\int_0^\pi \int_{-\infty}^0 \hat{f}(r\vec{\eta}_\theta)e^{ir\langle\vec{\eta}_\theta,\vec{x}\rangle}(-r)\,\mathrm{d}r\,\mathrm{d}\theta$$

$$f(\vec{x}) = \frac{1}{(2\pi)^2}\int_0^\pi \int_{-\infty}^\infty \hat{f}(r\vec{\eta}_\theta)e^{ir\langle\vec{\eta}_\theta,\vec{x}\rangle}|r|\,\mathrm{d}r\,\mathrm{d}\theta$$

Using the Convolution Theorem and Fourier Slice Theorem in succession, the desired result is achieved:

$$f(\vec{x}) = \frac{1}{2\pi}\int_0^\pi (\mathcal{R}f(t,\theta)*h\langle\vec{x},\vec{\eta}_\theta\rangle)\,\mathrm{d}\theta \tag{7}$$

This equation bridges the gap from the tomographic projections, here represented by $\mathcal{R}f(t,\theta)$, to the attenuation coefficient associated with every point inside the sample ($f(\vec{x})$). Our choice for the scalar field $h(\vec{x},\vec{\nu}_\theta)$ is free, which makes it possible to take advantage of that flexibility in defining h, treating it as a filtering function to sharpen the image or remove aberrations. Using the Convolution Theorem in this way both makes the whole process more computationally feasible and easier to tune.

2.3 Kinds of Tomography

In a neutron imaging set up, a beam of neutrons is shot at a sample which absorbs or deflects some of the neutrons according to the attenuation coefficient. The remaining neutrons that pass through the sample are then measured by a neutron detector, which is translated to a visual map that shows the number of neutrons that hit the detector in each area by the brightness. The neutron beam is usually collimated, filtering out neutrons that are not traveling perpendicular to the detector. This is used to reduce blurring of the image. This is also influenced by the distance between the beam source, sample object and detector, as the neutrons will have some variation in their direction of travel. The number of neutrons that pass through the sample and hit the detector is found by taking the path integral of the attenuation coefficient, where the path is the path of the neutron beam. This physical process is equivalent to taking the Radon transform of the attenuation properties of the inside of the sample. More simply, the fraction of the beam lost through each portion of the material as the beam passes through is summed through the entire material to find the beam intensity upon the detector.

Neutron attenuation is primarily influenced by the nucleus of the sample atoms, and hence the elements and isotopes present in the sample material. The spatial density of the sample atoms will influence the attenuation. This means that different states of matter and crystalline structures in solids will have different attenuation. However, in this project's sample, the crystalline structures are small and randomly oriented and thus their net effect on the attenuation coefficient is negligible.

When imaging, a variety of neutron energies are permissible, and these neutron energies are sometimes referred to as their temperature. "Cold", "thermal", or "epithermal" neutrons refers to the kinetic energy of a neutron relative to neutrons with a characteristic energy of 300K, or about room temperature. This is relevant because this energy is also the kinetic energy of a beam of neutrons that has been filtered through a moderator at room temperature [Arai and Crawford, 2009]. Respectively, cold, thermal, and epithermal neutrons have energies less than, equal to, and greater than this, with additional categories further out on the extremes. Here only cold and thermal neutrons will be considered, which have energies of 0.001-0.024eV and 0.025eV.

Other imaging techniques provide complimentary information to NCT. X-ray micro-computed

tomography (XμCT) is also a tomography technique, in that there is some source of radiation, a detector, a sample in between, and projections are taken through the sample to learn about its properties. The sample attenuates the radiation via absorption and scattering of the radiation, and this can be measured at the detector with knowledge of the original source. These attenuation images are taken from many different angles, and reconstructed tomographically. XmuCT differs from NCT in that X-rays interact with the outermost electron shell of the atoms in the material, and so the attenuation characteristics of a material are directly associated with the atomic numbers (Z) of its component atoms, rather than the properties of the nucleus [Karch et al., 2017]. X-rays are also much easier to produce at scale than neutrons, and so XmuCT can attain a much higher spacial resolution than NCT.

3 Methods

3.1 Fossil Properties

When analyzing the sample, the paleontologists at the Aathal Dinosaur Museum found that the fossil matrix material is made of sandstone, the typical rock found in the Morrison formation. They also found that the bone itself is made of agate, pyrite, and hydroxyapatite. The fossils were painted in patches of hydrogen-rich cyanoacrylate to improve their structural integrity and for ease of transport. Great care was paramount to ensure that the contrast provided by the cyanoacrylate and the contrast provided by the bone material were distinguishable.

The Museum trimmed fossils A-D down so that they could be imaged more easily, as leaving extra matrix material around the bone diminishes the contrast. Fossil C broke into two pieces in transit, which will be referred to as C1 and C2, going from left to right in Figure 1. Each sample was affixed on the beamline turntable either using a weak adhesive, if the sample was short and light enough that this would prevent wobbling, or by temporarily gluing an aluminum cylinder to the platform, placing the sample inside, and packing the cylinder tightly with aluminum foil to keep the sample stationary as the turntable rotated. Each sample was positioned so that the part of the sample intended for imaging was clear of the aluminum tube, so that neutron attenuation through the aluminum would not damage the images. Sample D was affixed in the beamline using a larger aluminum cylinder, but was otherwise prepared the same way.

Sample A was imaged a second time after washing it with acetone to remove the cyanoacry-

late painted onto its surface. There was hope that this would make it easier to distinguish the cyanoacrylate from the spine and delicate rib structures in this sample. This second image is what was used for the final reconstruction.

3.2 X-ray Scanning

The first X-ray scans of sample A were taken at EMPA Dübendorf. An EasyTom XL Ultra 230-160 micro/nano-CT scanner was used, containing a Hamamatsu reflection type micro-focus X-ray tube, and using a 0.35mm thick copper plate over the aperture to prevent beam hardening. The sample was too long and thin to get a good close image with the entire sample in their field of view, so a helical scan was taken with a total of 4628 projections over 4 full turns of 360 degree; this results in 1157 projections per turn taken. The detector for the scans was a Varian PaxScan 2520DX detector (flat panel with amorphous silicon and a CsI converter, 1920 x 1536 pixel matrix; pixel pitch of 127 mm; 16 bits of dynamic range). With these parameters, a voxel size of 28.44 um in the resulting CT image was achieved. Each projection that was eventually fed to MuhRec is derived from 15 images averaged together, taken at a rate of 7 frames per second. A few slices taken from a later X-ray tomography reconstruction of this sample are depicted in Figure 7

X-ray scans were taken of samples B and C2, as well as additional scans of sample A on the NEUTRA beamline, using the XTRA option available there. XTRA uses a GE ISOVOLT-Titan 320 X-ray source, with a Andor Neo sCMOS digital camera and 100 μm Lithium Fluoride/Zinc Sulfide scintillator screen though the sample was only imaged at 160 keV and not the full 320 keV the X-ray source tube was capable of. X-ray tomography projections were taken through a full 360° rotation, from 625 different angles. Each image was exposed for 6 seconds, and 3 images were taken at each angle, for a total of 1878 images (the additional three is from imaging at the same angle twice 360° and 0° at the beginning and end, for 626 sets of 3 images). The sample was set in the beam as close to the scintillator screen as possible without the sample brushing it as it rotates. Each sample was oriented somewhat differently in the frame due to their different sizes and shapes, so they could be positioned manually via the external computer system by moving the sample, taking a short exposure, and verifying that the sample was well-centered in the image, repeating this process until satisfactory.
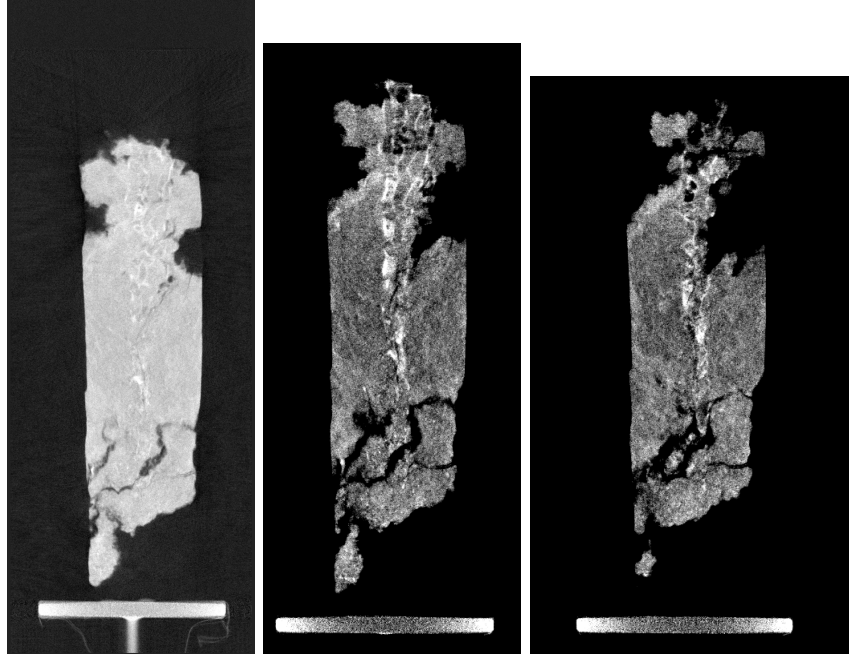
Figure 7: Slices through Sample A, taken using X-rays.

Samples B and C2 were imaged with X-rays on the NEUTRA beamline, which allows for X-ray tomography to be done in the exact same positions and exact same angles, with similar optical properties for a given sample. The X-ray source was used at 160 keV, and took images through the full 360° using 625 distinct angles, and 3 images taken per angle. Each image had an exposure time of 6 seconds.

3.3 Neutron Scanning

After each sample was prepared, it was placed on the turntable in the NEUTRA beamline, and the imaging process began. For the neutron projections, the same number of angles and scans were used as when doing X-ray tomography, but each image was exposed for 30 seconds instead of 6 seconds. When planning out how long was needed to wait for the images to complete an additional 20% was added to the naive estimate of 15:40 minutes to account for times where the neutron flux was low, and no images were taken. Samples A and B were scanned without incident, but Sample C2 required two passes, as the portion of the sample of interest extended past the bounds of the 10cm x 10cm field of view. Sample D was very large, but had comparatively less interesting bone inside, so only the most interesting portion was imaged in front of the 13cm x 13cm view

port. After imaging Sample D, Sample A was imaged a second time after rinsing the cyanoacrylate from it. This was in order to see how far the glue penetrates into the material when used, and in addition, ribs were present in the first neutron imaging of this sample, but their shape was blurred by the glue. This made them more clearly visible.

3.4 Image Processing

Several software packages were used to process and visualize the data after collection from the scans. ImageJ is a free-to-use, open source image processing software developed by the NIH [Carminati and Kaester, 2017]. It has functionality for cropping, transformations, and filtering on individual images as well as series of images, which makes it useful for processing data in 3D image form. MuhRec is a computational program for computer tomography developed in-house at PSI. MuhRec has capabilities for identifying the tilt of sample rotation, subtracting both open beam and dark current, and it allows for different filtering processes used during reconstruction. KipTool is an open-source software project that exists as part an international github collaboration between beam scientists. The primary contributors to this project are Dr. Anders Kaestner of PSI and Dr. Wojciech Potrzebowski of Lund University. It uses blackbody images taken during scanning to reduce noise from background radiation before tomographic reconstruction. Avizo is a proprietary 3D imaging and processing software made by ThermoFisher Scientific. It is capable of various data manipulations, such as segmentation, cleaning, and visualization of 3D data.

Images taken on NEUTRA were pre-processed in ImageJ by taking the median of the dark current images made for that scan, subtracting them from all other images, and then removing bright outliers caused stray gamma rays using the remove outliers tool, with a radius of 4 pixels and brightness difference of 300. As mentioned in previous sections, there were three projections for each scanning angle used. These three images are averaged together, as were all the open beam images, producing a single open beam image. This is done for the open beam images taken both with and without blackbodies. Those blackbody images taken with the sample in the beam to determine scattering effects were averaged together in groups of three in the same fashion as the projections.

MuhRec uses similar mathematics as to what was described in Section 2.2 to extract

attenuation coefficients for each point in a given sample. It additionally uses the convolution as an opportunity for preprocessing the data, adds corrections for cone-beam geometry(as no beam is perfectly collimated and parallel), and various options for postprocessing of the reconstruction to remove streaks, ring aberrations, and blurriness.

MuhRec requires open beam images, dark current images, and projections to do its reconstruction. MuhRec's means of removing the dark current is less effective than what has already been done in ImageJ, so instead of letting MuhRec remove the dark current, it was removed earlier and here MuhRec is fed a perfectly blank image with zero values everywhere for its dark current image. These were made in ImageJ arithmetically by multiplying the image by zero. The data followed the naming scheme MuhRec uses by default, with a prefix indicating the purpose of the image followed by indices. The dark current images were named similarly and were placed in the same folder. This enables MuhRec to easily locate all of the necessary images during the reconstruction.

Some of the pre-processing modules present in MuhRec were used: BBLogNorm or FullLogNorm options, depending on if blackbodies were being used or not, MorphSpotClean, and WaveletRingClean. There was no need to use any back-projection modules other than the default MultiProjBPparallel because NEUTRA's beam is close enough to parallel to make cone beam geometry modules less useful. Each time a reconstruction was done, it was imperative to adjust for an off-center axis of rotation. Even an apparently flawless turntable can be off-center enough to introduce obvious circular aberrations into the reconstruction slices. The portion of the sample was selected that exhibited the least effects of precession and extrapolated the axis of rotation from the data in that portion in MuhRec.

MuhRec reconstructs the tomography images into slices taken perpendicular to the axis of rotation, which are then optionally fed into KipTool before finally getting loaded into Avizo. KipTool was used to do blackbody corrections for excessive scattering of neutrons as they passed through the sample. The blackbodies are small cylinders of boron carbide which absorb all or essentially all neutrons that pass through them, so an image taken with these blackbodies present should have patches in them that are perfectly black aside from the dark current. Any neutron scintillation detected in these portions of the image must be from scattering inside the sample, and should be subtracted out. What is subtracted is not simply those detections in the part of the
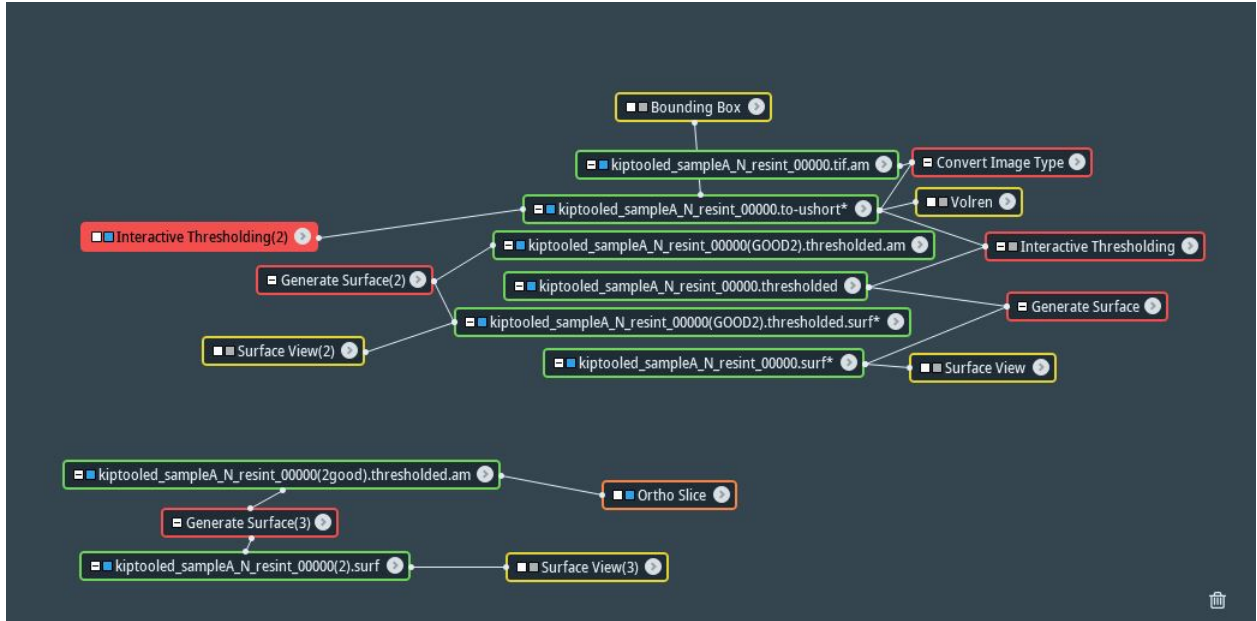
Figure 8: Example of an Avizo workspace for visualization and segmentation of sample A.

image with the blackbodies. KipTool extrapolates from these patches to cover the entire region of interest in the image, and it is this extrapolated scattering effect that is removed from the image. However, it quickly became clear that the corrections were imperceptible for samples as thin as these. Only blackbody corrections on sample C were attempted, and these corrections were not retained in the final product.

From MuhRec or KipTool, the reconstruction slices were moved to Avizo. In Avizo the data was first converted to unsigned 16-bit integer instead of the floating point values MuhRec prefers to produce. Immediately, an intensity threshold for the images was set that best distinguished the bones or other interesting structures from the surrounding material. This produces a thresholded image that can be used to generate a surface, and it is this surface used as the segmentation of the data. The surface is the boundary between those points in the image above and below the threshold, and depending on the intensity threshold chosen, one can select various features of the image. A very permissive threshold was selected to get the outside surface of the sample, and a more restrictive threshold to bring the internal structure into relief. An Avizo workflow for performing the above process once is depicted in Figure 8. Once this has been done, these surfaces are cleaned up to create a 3D model of the bone and matrix components of the sample. These models are the final product.

The clean up process made up a plurality of the labor in this project. All extraneous sources of attenuation visible in the segmentation that are not bone, attached to bone, close to bone, or roughly where bone should be needed to be removed using Avizo. Small extraneous regions in the segmentation are called islands, and Avizo has a tool specifically for removing these. For those regions clearly unrelated to the structure of the bone, the Lasso tool enables us to select cylinders cutting through the model to be excluded from it. These are the primary tools used to clean up the segmentations, and the limitations of this process are visible in some of the visualizations present in Section 4.2.

4 Results

4.1 Reconstructions

Tomographic reconstructions were built of all samples but C1. NCT reconstructions were made of samples A, B, C2, and D, and XμCT reconstructions of samples A and B. The projections from each of the X-ray and neutron scans were quite clear, which enabled a more straightforward reconstruction of the samples chosen. Images to compare the NCT and XμCT scans of sample A are shown in Figure 9. Sample A was scanned four times–twice with the cyanoacrylate still present on and in the sample, in both neutrons and X-rays, and twice after washing with acetone to remove the cyanoacrylate. Sample B was scanned two times, once with X-rays and once with neutrons, and samples C2 and D were only scanned a single time. Every scan taken was reconstructed, but ultimately only the reconstructions with the best contrast and most useful features for each sample were used, which would be the washed NCT reconstruction of sample A and the NCT reconstruction of sample B. The single scans taken of samples C2 and D were also used.

The XμCT reconstructions universally suffered from poor contrast between the sandstone matrix and hydroxyapetite fossil structure. While there are slight differences in density and X-ray attenuation between the two, the contrast achieved was slight in comparison to the stark differences seen with the neutrons. Reconstructions of samples B and D appeared to have very little fossil in them, and this persisted into the segmentations. Sample A was easily the best reconstruction, with ribs and vertebrae clearly visible even at this stage in the process, and persisting all the way
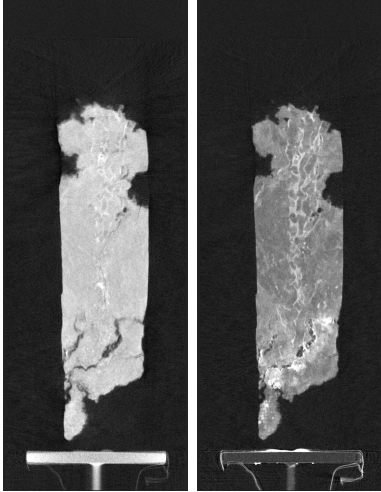
22

Figure 9: A side by side comparison of NCT and XµCT reconstructions of sample A.
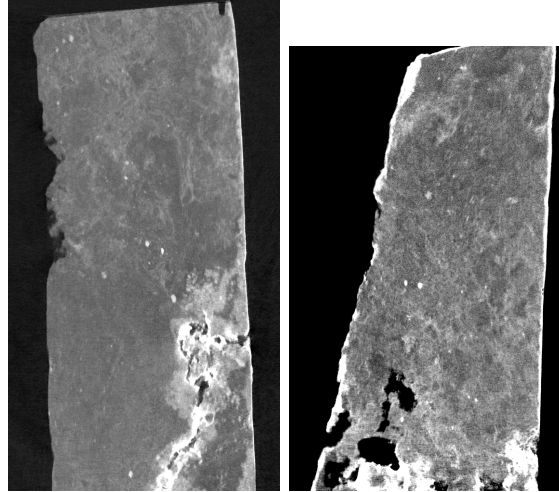

Figure 10: NCT reconstruction slices of sample B and D.

into the final visualizations. Example slices of samples B and D are shown in Figure 10. These were the slices that seemed to have the clearest evidence of vertebrae in them. This fact was very concerning until later in the modeling process, when the positions of the samples as they would have been underground were recreated, showing that the bones present in samples A and C link up neatly with no missing sections as the vertebral column passes through B and D. 3D models of the samples arranged in this fashion are described in Section 4.3.

4.2   Segmentations

Several 3D models were segmented from the NCT reconstructions in Avizo, some of which were used as is, and others which required additional processing before they could be used in a visualization. For each sample brightness thresholds were set, dividing the material of interest from the material that was not. The entire fossil was segmented out first, so that a 3D model of the exterior of the fossil could be used to juxtapose against any bone found inside. One such exterior model is found in Figure 11. Afterwards, the bone was segmented out from the surrounding sandstone in samples A and C, as no bone was found in samples B or D, as discussed above.

Unlike the fossil exterior segmentations, the bone segmentations were not usable immediately after segmentation. The sandstone is impregnated with cyanoacrylate creating blobs of contrast in the sample close to the surface, and there is a reasonable amount of noise present all
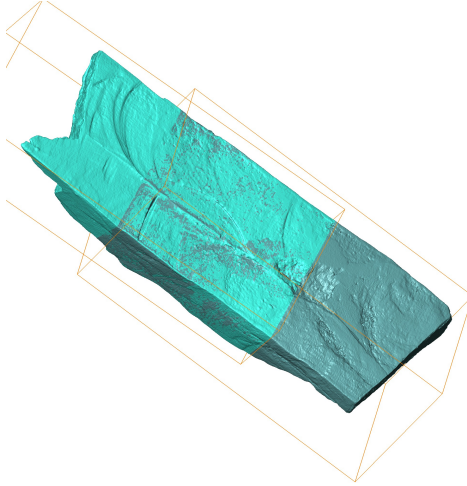
Figure 11: Composite model of sample C2 constructed from two separate models.

Figure 12: A 3D model of the vertebral column present in samples A and C.

around. Once the segmentation was complete, the model also needed to be cleaned, removing obvious noise and blobs of glue from the model. The resulting bone models are visible in Figure 12, color-coded to show that the two sections come from different samples.

4.3 Visualizations

As mentioned in the previous section, once all four samples were segmented, blobs of resin and inclusions in the sandstone which were not of concern had to be cleaned away from the model. Avizo's Island detection software and Lasso tool were used to remove sections that were clearly neither attached to/part of the bone nor large enough to potentially be a bone themselves. This was only a concern for segmentations and models one might find on the interior of a fossil sample. In contrast, the segmentations displaying the exterior of the samples were immediately useful in marking how the samples fit together, and these were used to rearrange the 4 samples as they would have been prior to being unearthed. These are the tools we used to make Figure 13. With this model, the segmentations in question could be matched up and and used to confirm that everything was found before fully devoting time to cleaning up the models.

Once cleaned, the models of the bones were set into the transparent exterior models of samples A and C, like in Figure 14.
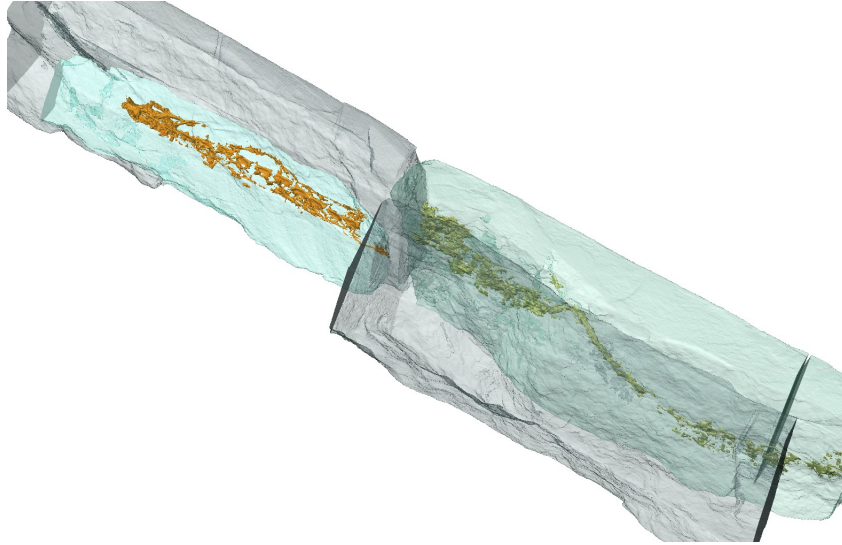
Figure 13: A holographic image of all 4 samples arranged as they would be underground.

4.4 Fossil Identification

The 3D visualizations were presented to Dr. Yolonda Schicker-Siber and Dr. Hans-Jakob Siber of the Aathal Dinosaur Museum. They were not able to conclusively identify the fossilized creature, however, they were able to make some preliminary observations. They were able to conclude that the fossil is not a snake, as there are ribs running along only a portion of the spine, not the whole length. They were also able to point out a possible pelvis and skull, however these would need further investigation and expertise to identify conclusively.

From this initial presentation of the 3D model, they were also able to say the fossil was likely complete as was a completely intact spine and ribs and it would be unlikely that there would be an intact spine but no traces of any limbs if the creature did in fact have legs. For a creature with limbs, it would be highly unlikely for the entire spine to fossilize and none of the limbs to fossilize at all.

There are two main lines of further investigation, either this is a complete fossil and a currently undiscovered creature, not a snake, which has no limbs. This creature would be as of yet unidentified. Another possibility for the original creature is that it was extremely young at time of death. This would explain some of the odd things seen, as such young creatures have not fully calcified their skeletons, and the cartilaginous sections of their skeleton would decay more easily,
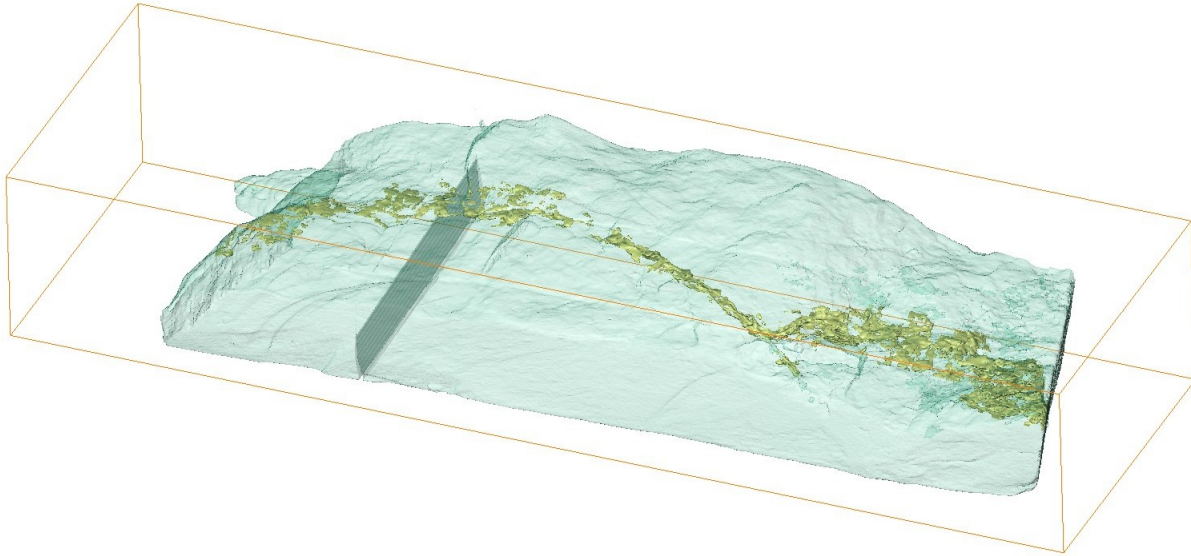
25

Figure 14: Holographic 3D model of sample C with vertebral column.

leaving behind no visible traces of hydrogen. However, this does not explain the simultaneous presence of a complete spine and non-presence of even partial limbs or a well-defined head. It would be odd for the spine to be totally calcified but the limb bones to be mostly soft tissue.

The Museum is going to bring more expertise on board and spend more time examining the fossil visualizations. The hope is that this additional effort will enable them to resolve the above confusions and provide a final identification of the fossil, or at least narrow the possibilities down to a short whitelist of possibilities.

5 Conclusion

In this report, we have presented the output of a project undertaken at the Swiss Spallation Neutron Source (SINQ) of the Paul Scherrer Institute. The goal was to perform NDT on a unique fossil that appears to be a set of bones and ribs of some unknown pre-historic animal that is embedded in a sandstone block. The fossil was found in the Morrison formation in Wyoming by the expedition of the Swiss Aathal Dinosaur Museum, and they had significant difficulties in identification of the animal using conventional techniques. The tested block was imaged with the use of neutron computed tomography and post-processed with special computational tools (ImageJ, Muhrec, and Avizo) used at PSI for reconstruction of images from neutron contrasts.

In the course of reconstruction, while shape of the bones inside samples A and C were extracted, noise was visible in the tomography reconstructions of every sample. This noise didn't necessarily come from aberrations but from objects within the material. There was visible attenuation from the hydrogenated resin, and this was removed from the final models. There were no large shapes or bone structures in samples B or D, and the alignment of the bones in A and C confirms this. There was a single continuous vertebral column running the breadth of the samples, missing both B and D, with ribs along the section in sample A.

Eventually, a high-resolution 3D holographic image of the sandstone block with the embedded vertebral column was successfully obtained. The picture seems to be showing all parts of bones and ribs hidden inside the sandstone block. However, the image was found by the Aathal Dinosaur Museum to be inconclusive: it was not possible to identify the animal behind this fossil

based on the visible set of bones. The image, along with the materials documenting the process of visualization, was passed to the Museum for more detailed investigation and identification of the pre-historic animal with the help of external expertise.

References

[Arai and Crawford, 2009] Arai, M. and Crawford, K. (2009). Neutron Sources and Facilities. In Bilheux, H. Z., McGreevy, R., and Anderson, I. S., editors, *Neutron Imaging and Applications*, Neutron Scattering Applications and Techniques. Springer US, Boston, MA.

[Bevitt, 2018] Bevitt, J. J. (2018). Discovering dinosaurs with neutrons. *Nature Reviews Materials*, 3(9):296–298.

[Bilheux et al., 2015] Bilheux, H., Santodonato, L., Bilheux, J., and Bailey, B. (2015). Introduction to Neutron Radiography and Computed Tomography. lecture slides.

[Caldwell et al., 2015] Caldwell, M. W., Nydam, R. L., Palci, A., and Apesteguía, S. (2015). The oldest known snakes from the Middle Jurassic-Lower Cretaceous provide insights on snake evolution. *Nature Communications*, 6(1):5996.

[Candes, 2021] Candes, P. E. (2021). Applied Fourier Analysis and Elements of Modern Signal Processing: Lecture 10. https://candes.su.domains/teaching/math262/Lectures/Lecture10.pdf. Accessed: 2023–12-15.

[Carminati and Kaester, 2017] Carminati, C. and Kaester, A. (2017). MuhRec – a reconstruction tool for neutron and x-ray tomography. In *The 3rd International Conference on Tomography of Materials and Structures*, Lund, Sweden.

[De Beer, 2017] De Beer, F. C. (2017). Paleontology: Fossilized Ancestors Awaken by Neutron Radiography. In Kardjilov, N. and Festa, G., editors, *Neutron Methods for Archaeology and Cultural Heritage*, Neutron Scattering Applications and Techniques, pages 141–171. Springer International Publishing, Cham.

[Grellet-Tinner et al., 2011] Grellet-Tinner, G., Sim, C. M., Kim, D. H., Trimby, P., Higa, A., An, S. L., Oh, H. S., Kim, T., and Kardjilov, N. (2011). Description of the first lithostrotian titanosaur embryo in ovo with Neutron characterization and implications for lithostrotian Aptian migration and dispersion. *Gondwana Research*, 20(2-3):621–629.

[Karch et al., 2017] Karch, J., Dudák, J., Žemlička, J., Vavřík, D., Kumpová, I., Kvaček, J., Heřmanová, Z., Šoltés, J., Viererbl, L., Morgano, M., Kaestner, A., and Trtík, P. (2017). X-ray micro-CT and neutron CT as complementary imaging tools for non-destructive 3D imaging of rare silicified fossil plants. *Journal of Instrumentation*, 12(12):C12004–C12004.

[Laaß, 2015a] Laaß, M. (2015a). Bone-conduction hearing and seismic sensitivity of the Late Permian anomodont Kawingasaurus fossilis. *Journal of Morphology*, 276(2):121–143.

[Laaß, 2015b] Laaß, M. (2015b). Virtual reconstruction and description of the cranial endocast of Pristerodon mackayi (Therapsida, Anomodontia). *Journal of Morphology*, 276(9):1089–1099. _eprint: https://onlinelibrary.wiley.com/doi/pdf/10.1002/jmor.20397.

[Laaß et al., 2017] Laaß, M., Schillinger, B., and Werneburg, I. (2017). Neutron Tomography and X-ray Tomography as Tools for the Morphological Investigation of Non-mammalian Synapsids. *Physics Procedia*, 88:100–108.

[PSI, 2023] PSI (2023). Neutron Tomography | NIAG | Paul Scherrer Institut (PSI).

[Pugliesi et al., 2019] Pugliesi, R., Pereira, M. A. S., Andrade, M. L., Basso, J. M., Voltani, C. G., and Gonzales, I. C. (2019). Study of the fish fossil Notelops brama from Araripe-Basin Brazil by Neutron Tomography. *Nuclear Instruments and Methods in Physics Research Section A: Accelerators, Spectrometers, Detectors and Associated Equipment*, 919:68–72.

[Schillinger et al., 2018] Schillinger, B., Beaudet, A., Fedrigo, A., Grazzi, F., Kullmer, O., Laaß, M., Makowska, M., Werneburg, I., and Zanolli, C. (2018). Neutron Imaging in Cultural Heritage Research at the FRM II Reactor of the Heinz Maier-Leibnitz Center. *Journal of Imaging*, 4(1):22.

[Schillinger et al., 2000] Schillinger, B., Lehmann, E., and Vontobel, P. (2000). 3D neutron computed tomography: requirements and applications. *Physica B: Condensed Matter*, 276-278:59–62.

[Siber, 2023] Siber, H.-J. (2023). personal correspondence. email.

[Treimer, 2009] Treimer, W. (2009). Neutron Tomography. In Bilheux, H. Z., McGreevy, R., and Anderson, I. S., editors, *Neutron Imaging and Applications*, Neutron Scattering Applications and Techniques. Springer US, Boston, MA.